

Simulated prosthetic vision identifies checkerboard as an effective raster pattern for retinal implants

Justin M. Kasowski¹ and Michael Beyeler^{2,3}

¹Interdepartmental Graduate Program in Dynamical Neuroscience, University of California, Santa Barbara, CA, 93106

²Department of Computer Science, University of California, Santa Barbara, CA, 93106

³Department of Psychological & Brain Sciences, University of California, Santa Barbara, CA, 93106

E-mail: mbeyeler@ucsb.edu

Abstract. *Objective:* This study systematically evaluates the impact of raster patterns—specific spatial arrangements of sequential electrode activation—on performance and perceived difficulty in simulated prosthetic vision (SPV). By addressing a critical gap in the literature, we aimed to identify patterns that optimize functional vision in retinal implants.

Approach: Sighted participants completed letter recognition and motion discrimination tasks under four raster patterns (horizontal, vertical, checkerboard, and random) using an immersive SPV system. The simulations employed psychophysically validated models of electrode activation, phosphene appearance, and temporal dynamics, ensuring realistic representation of prosthetic vision. Performance accuracy and self-reported difficulty were analyzed to assess the effects of raster patterning.

Main Results: The checkerboard pattern consistently outperformed other raster patterns, yielding significantly higher accuracy and lower difficulty ratings across both tasks. The horizontal and vertical patterns introduced biases aligned with apparent motion artifacts, while the checkerboard minimized such effects. Random patterns resulted in the lowest performance, underscoring the importance of structured activation.

Significance: These findings provide the first systematic evaluation of raster patterns, suggesting that the checkerboard configuration may enhance usability and perceptual clarity in retinal implants. While based on simulated environments, this study establishes a foundation for optimizing spatial and temporal electrode activation strategies in next-generation devices.

Keywords: prosthetic vision, raster patterns, letter recognition, motion discrimination, virtual reality, eye tracking, retinal prostheses

1. Introduction

Retinal degenerative diseases, such as retinitis pigmentosa (RP) and age-related macular degeneration, are major causes of severe vision loss, often diminishing quality of life and personal independence (Hamel, 2006; Sainohira et al., 2018; Prem Senthil et al., 2017). While early-stage RP may benefit from emerging treatments like gene and stem cell therapies (Russell et al., 2017; da Cruz et al., 2018), electronic visual prostheses remain a critical option for individuals in the advanced stages of degeneration (Beyeler et al., 2017b).

Visual prostheses function by capturing visual input, typically with an external camera, and converting it into electrical signals delivered to implanted microstimulators (Weiland et al., 2016; Fernandez, 2018). These devices stimulate surviving neurons in the retina or visual cortex, evoking the perception of phosphenes—flashes of light. Among retinal devices, the Argus II Retinal Prosthesis System (Vivani Medical, Inc.; formerly Second Sight Medical Products, Inc.) was the first to achieve regulatory approval (Luo and da Cruz, 2016) and has been implanted in 388 individuals worldwide (personal communication with Cortigent, Inc., 2024). Currently nearing commercialization is PRIMA (Lorach et al., 2015; Palanker et al., 2020), a compact subretinal implant with a photovoltaic design that eliminates the need for external cables. Originally commercialized by Pixium Vision, the technology has since been acquired by Science Corporation, which is now advancing its development. Meanwhile, cortical prostheses with higher electrode counts are being developed to bypass the retina entirely, potentially providing a treatment option for a wide range of blindness causes (Chen et al., 2020; Jung et al., 2024; Musk and Neuralink, 2019).

Advancing high-resolution prostheses presents significant challenges. Safety guidelines established by regulatory agencies, such as those from the US Food and Drug Administration (FDA), limit the number of electrodes that can be activated simultaneously or in close succession to prevent adverse events, neural damage, and electrode degradation. While these constraints are essential, they also hinder the resolution required for complex functional tasks.

One strategy to address these limitations involves preprocessing the visual input, using methods like edge detection or semantic segmentation to simplify scenes and emphasize task-relevant features (Parikh et al., 2010; Vergniewux et al., 2017; Sanchez-Garcia et al., 2020; Han et al., 2021). Although preprocessing may enhance perceptual clarity by emphasizing salient or task-relevant features of the scene (Beyeler and Sanchez-Garcia, 2022), safety constraints still necessitate activating only a subset of electrodes at any given moment.

Existing prostheses, such as the Argus II, address this by activating subsets of electrodes (“timing groups”; Second Sight Surgeon Manual, 2013) in rapid temporal succession. Inspired by raster scanning in display technologies, this approach sequentially segments the visual field into strips, aiming to create the perception of a coherent visual frame. Raster patterns, which define the spatial arrangement

and activation order of these electrode groups, are typically chosen randomly or adjusted heuristically based on limited user feedback (Second Sight, 2013). While these approaches address safety concerns, they lack systematic evaluation, leaving open questions about how specific patterns influence perceptual and behavioral outcomes. This is particularly relevant as both retinal and cortical implants evolve to include hundreds or thousands of electrodes.

To date, no systematic studies have assessed the impact of raster patterns on task performance. Conducting such research with real prosthesis users is challenging due to variability in device functionality, individual neuroanatomy, and patient-specific factors. Simulated prosthetic vision (SPV) in immersive virtual reality (VR) offers a controlled alternative, enabling experiments with “virtual patients” in realistic environments (Hayes et al., 2003; Dagnelie et al., 2007; Kasowski and Beyeler, 2022). The validity of these simulations depends on accurate modeling of electrode activation (Kasowski and Beyeler, 2022), phosphene appearance (Beyeler et al., 2019; Granley and Beyeler, 2021), and temporal dynamics (Hou et al., 2024b), making realism a critical aspect of SPV research.

In this study, we systematically evaluated four raster patterns—horizontal, vertical, checkerboard, and random—using SPV to assess their effects on letter recognition and motion discrimination tasks. By analyzing task performance and perceptual biases across these configurations, we aimed to identify patterns that optimize usability while adhering to regulatory safety constraints.

As high-resolution prosthetic technologies for retinal and cortical applications continue to develop, refining electrode activation strategies will be essential to bridge the gap between engineering advancements and the practical needs of individuals with vision loss (Nadolskis et al., 2024). Simulated experiments like this study represent an important step toward refining these systems and advancing their clinical viability.

2. Methods

2.1. Participants

We recruited 48 participants with normal or corrected-to-normal vision (ages 18–29; $M = 19.71$, $SD = 2.72$; 28 female, 20 male) from the Department of Psychological & Brain Sciences research participant pool at the University of California, Santa Barbara (UCSB). Participants served as “virtual patients” (Kasowski and Beyeler, 2022) in simulated prosthetic vision experiments. Ten participants had never used VR before. To minimize the risk of cybersickness or discomfort, participants prone to light sensitivity or flashing lights were excluded. The study was approved by UCSB’s Institutional Review Board.

2.2. Simulated prosthetic vision (SPV)

We used the open-source Unity toolbox `BionicVisionXR` (Kasowski and Beyeler, 2022) to simulate prosthetic vision in an immersive VR environment. Participants viewed stimuli through an HTC VIVE Pro Eye head-mounted display, with phosphene appearance simulated using psychophysically validated models (Horsager et al., 2009; Beyeler et al., 2019; Granley and Beyeler, 2021). This approach modeled spatiotemporal dynamics and gaze-contingent rendering (explained further below) to approximate the visual experiences of retinal prosthesis users.

To maintain generalizability while aligning with near-future technologies, we simulated a 10×10 epiretinal electrode array centered over the fovea, inspired by the Argus II implant (Luo and da Cruz, 2016). Electrodes were simulated as point sources with $400 \mu\text{m}$ spacing. Scene content dynamically updated based on participants’ head and eye movements, providing a realistic approximation of user interaction with prosthetic vision.

2.3. Raster patterns

Visual prostheses must adhere to strict safety guidelines, including limits on electrode charge density and simultaneous current. These restrictions ensure safety but typically prevent all electrodes from being activated simultaneously. To comply, implants such as the Argus II divide electrodes into “timing groups” (Second Sight Surgeon Manual, 2013), stimulated in rapid succession. For this study, we use the term *raster pattern* to refer to the spatial arrangement and activation sequence of these timing groups, analogous to raster line scanning in display systems.

To systematically evaluate performance under different raster patterns, we tested four configurations with varying spatial organization and randomness (Figure 1):

- **Horizontal:** Electrodes grouped in two adjacent rows, stimulated sequentially from top to bottom. This is believed to be equivalent to the default timing groups in Argus II (Second Sight Surgeon Manual, 2013).

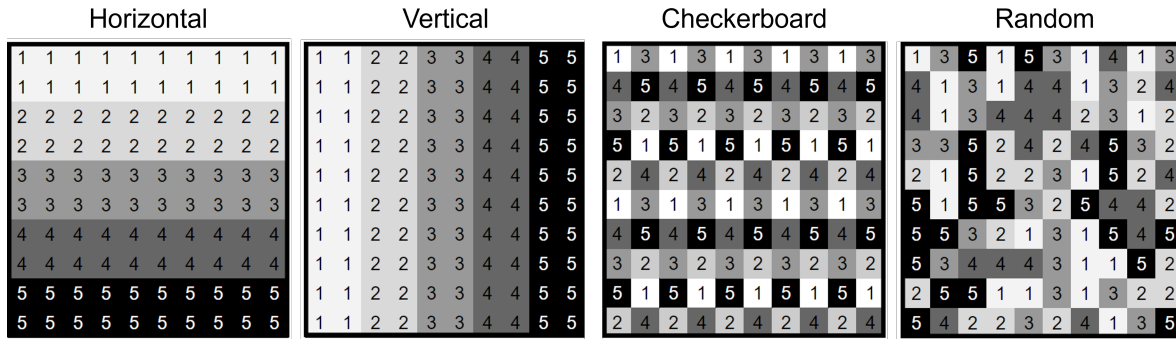


Figure 1: The four raster patterns tested in the study. Electrodes were divided into five timing groups (labeled 1–5) that were sequentially activated every 44 ms. *Horizontal:* Electrodes grouped into two adjacent rows, activated sequentially from top to bottom. *Vertical:* Electrodes grouped into two adjacent columns, activated sequentially from left to right. *Checkerboard:* Designed to maximize the distance between active electrodes. *Random:* Electrodes assigned to groups randomly at the start of each cycle.

- **Vertical:** Electrodes grouped in two adjacent columns, stimulated from left to right. This orthogonal arrangement allows for comparisons with the horizontal pattern and is designed to test whether raster directionality influences perceptual outcomes.
- **Checkerboard:** Electrodes were arranged to maximize spatial separation across successive activations, forming a checkerboard-like pattern. To transition between groups while avoiding apparent motion, the pattern was shifted using a non-linear strategy designed to preserve spatial separation. This approach minimized directional biases by avoiding simple linear shifts (e.g., one-pixel over) that could introduce apparent motion, instead ensuring each shift maintained balanced spacing and reduced perceptual interference between phosphenes.
- **Random:** Electrode activation randomized every five frames, with no fixed spatial structure to assess the importance of structured activation.

Each raster pattern activated 20% of the electrodes at a time, cycling through five distinct groups at 4.545 Hz. This raster frequency aligns with inter-pulse delays (25–83 ms) used in prior studies (Yücel et al., 2022), ensuring feasibility while remaining general enough to apply to next-generation prosthetic designs.

When applied to a visual stimulus, the raster pattern divides the scene into discrete regions rendered sequentially by the electrode groups (illustrated in Figure 1). If the stimulation sequence is sufficiently rapid, temporal integration by the visual system may combine these fragments into a coherent percept (Rashbass, 1970; Efron, 1973). However, factors such as phosphene fading, persistence, and neural adaptation (Avraham et al., 2021; Hou et al., 2024b) complicate this process, and the influence of raster patterns on perceptual clarity and behavior remains unclear.

Supplemental Video 1 demonstrates a raster pattern with the temporal model enabled, while Supplemental Video 2 illustrates the same pattern without temporal

dynamics. Notably, the temporal model mitigates abrupt transitions between raster groups, producing a smearing effect that enhances perceptual smoothness. This distinction is critical, as vertical and horizontal patterns without the temporal model can appear jarring and visually uncomfortable, highlighting the importance of incorporating temporal dynamics in simulated prosthetic vision studies.

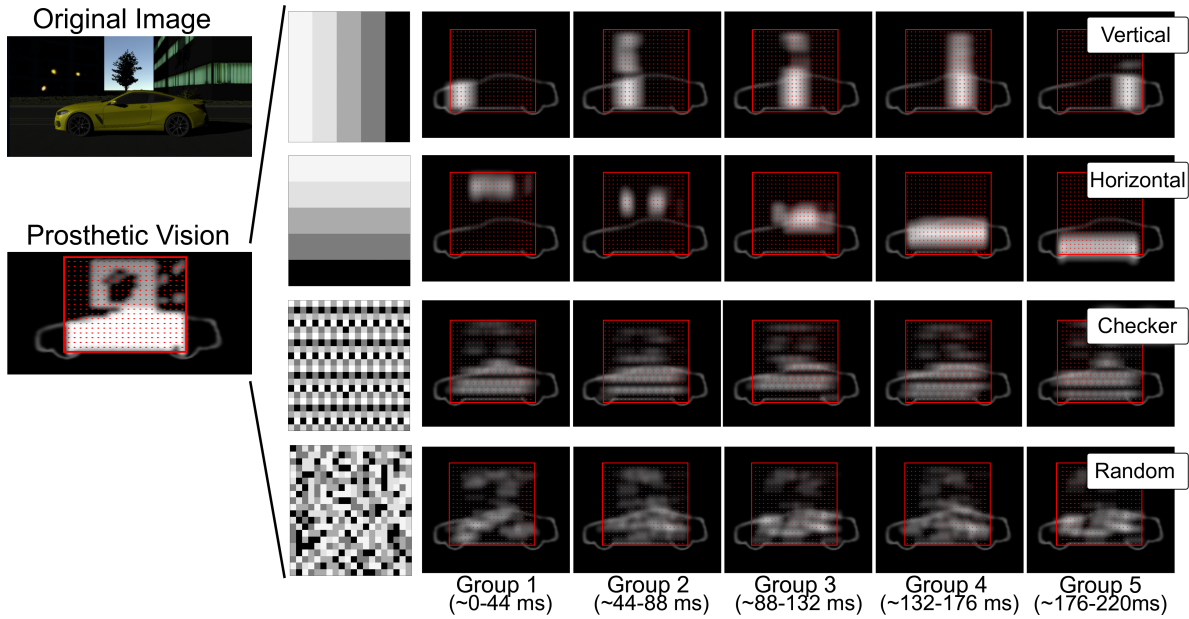


Figure 2: Raster patterns in simulated prosthetic vision. *Left:* The original image is converted into an electrode activation pattern for simulating prosthetic vision. Red dots in the “Prosthetic Vision” overlay indicate electrode locations. *Right:* To limit simulated current levels, the 100 electrodes were split into five distinct raster groups, indicated by the five gray levels in the leftmost panel. Four different raster patterns were tested: vertical (electrodes activate left to right), horizontal (top to bottom), checkerboard (maximally spaced electrodes across frames), and random (re-randomized every five frames). Groups were displayed at approximately 5 Hz to match the headset’s 11 ms (variable) frame timing.

2.4. Tasks

Two eight-alternative forced-choice tasks were designed to evaluate the effects of different raster patterns on visual performance:

- **Letter identification:** Modeled after Cruz et al. (2013); Kasowski and Beyeler (2022), participants viewed one of eight Snellen optotypes (C, D, E, F, L, O, P, T) subtending 41.112° of visual angle. Each joystick direction corresponded to a letter (e.g., forward-left for “C”), confirmed with a trigger button.
- **Motion discrimination:** Modeled after Dorn et al. (2013), participants viewed five-second videos generated using pulse2percept (Beyeler et al., 2017a), showing a single bar moving perpendicular to its orientation. Joystick directions indicated motion (e.g., forward-left for up/left), confirmed with a trigger button.

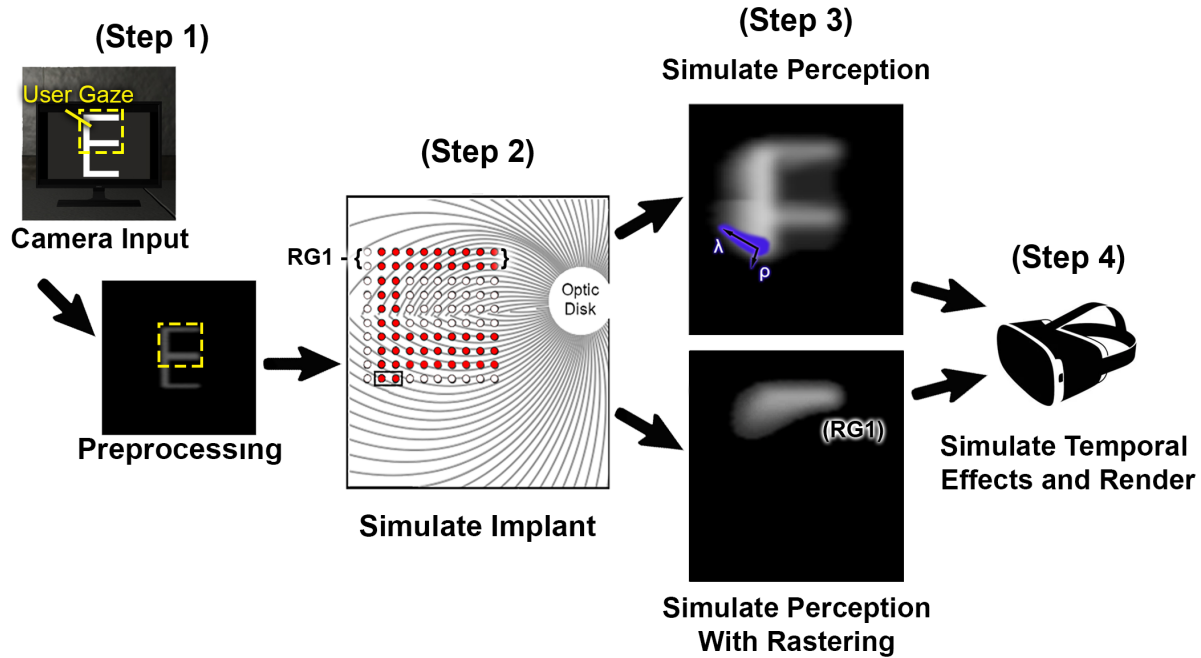


Figure 3: Simplified overview of the simulated prosthetic vision model. *Step 1:* Unity’s virtual camera captures the scene and preprocesses it (grayscale, Gaussian subsampling). *Step 2:* Electrode activation is determined based on the visual input as well as the placement of the simulated retinal implant. In the current study, a 3×3 Gaussian blur was applied to the preprocessed image to average the grayscale values around each electrode’s location in the visual field. This gray level was then interpreted as a current amplitude delivered to a particular electrode in the array. Electrodes are stimulated in close temporal succession according to their raster group; Raster Group 1 (RG1) electrodes are highlighted. *Step 3:* Perception is simulated either with (*bottom*) or without (*top*) rastering. Phosphene shape is determined by parameters ρ (spread) and λ (elongation). The highlighted shape represents the percept generated by two active electrodes in the horizontal raster condition, where only 20 out of 100 electrodes are active per frame. *Step 4:* Temporal dynamics are applied, and the final percept is rendered to the headset.

Both tasks were presented in a VR environment, with stimuli displayed on a virtual monitor in a darkened room. Each stimulus was shown for 5 s, during which participants could use head and eye movements to scan the scene. Participants selected their response using a joystick, with each of the eight directions corresponding to a specific choice. If no response was made during the stimulus presentation, the scene went black, and participants were required to make a decision. Immediate feedback (correct/incorrect) was provided after each trial, and participants had up to 5 s to finalize their response.

2.5. Simulation pipeline

The raster patterns were overlaid onto scenes, and visual input was processed through the following steps (Fig. 3):

1. **Image acquisition:** Unity’s virtual camera captured a 60° field of view, rendered

at 90 Hz.

2. **Image processing:** Frames were downsampled to 200×200 pixels, converted to grayscale, and smoothed with a 3×3 Gaussian kernel.
3. **Electrode activation:** Pixel intensities nearest to each electrode were used to compute activation levels. Only electrodes in the current raster group were stimulated (explained in Section 2.3).
4. **Spatial effects:** Phosphene shapes were modeled using the axon map (Beyeler et al., 2019; Granley and Beyeler, 2021), simulating elongated phosphenes aligned with retinal ganglion cell axons (Section 2.5.1).
5. **Temporal effects:** A temporal model (Horsager et al., 2009) simulated phosphene fading and persistence by accounting for charge accumulation and decay (Section 2.5.2).
6. **Gaze-contingent rendering:** The implant location dynamically shifted based on gaze position, ensuring the scene remained aligned with participants' fixation (Section 2.5.3).

This pipeline integrated spatial and temporal distortions to provide a realistic approximation of prosthetic vision (Kasowski and Beyeler, 2022).

2.5.1. Spatial distortions The shape of phosphenes in epiretinal devices is influenced by the retinal ganglion cell axons, which traverse the retina in curved paths (Rizzo et al., 2003; Beyeler et al., 2019). We used the axon map model to simulate these distortions (Beyeler et al., 2019; Granley and Beyeler, 2021). Each electrode activated a region of the retina defined by Gaussian falloff parameters ρ (spread) and λ (elongation). The instantaneous brightness b_I of each pixel (r, θ) in the percept was computed according to:

$$b_I = \max_{p \in R(\theta)} \sum_{e \in E} \exp\left(\frac{-d_e^2}{2\rho^2} + \frac{-d_{\text{soma}}^2}{2\lambda^2}\right), \quad (1)$$

where $R(\theta)$ is the path of the axon terminating at retinal location (r, θ) , p is a point along the path, d_e is the distance from p to the stimulating electrode e , and d_{soma} is the distance along the axon from p to the cell body. Values for ρ and λ were calibrated for each participant using a staircase procedure (Section 2.6).

2.5.2. Temporal distortions To model temporal dynamics, we used a simplified variant of the Horsager et al. (2009) model, which incorporates two coupled leaky integrators to simulate neural desensitization $n(t)$ and phosphene brightness $b(t)$. The governing equations were:

$$\frac{dn(t)}{dt} = -\tau_n n(t) + b_I(t), \quad (2)$$

$$\frac{db(t)}{dt} = -\tau_b b(t) - \alpha n(t) + b_I(t), \quad (3)$$

where $b_I(t)$ was the instantaneous brightness (from the spatial model) calculated at time t . Parameter values ($\tau_n = 0.2$ s, $\tau_b = 5$ s, and $\alpha = 0.2$) were fitted to reproduce temporal fading and persistence effects reported by Subject 5 (Figure 4) of Pérez Fornos et al. (2012).

2.5.3. Gaze-contingent phosphene rendering Participants’ eye movements were tracked using the HTC Vive Pro Eye. To ensure proper alignment between the simulated implant and the participant’s fixation point, the input image was first shifted to center the fixation point on the implant. This gaze-contingent rendering step enabled the subsequent simulation of temporal dynamics in retinal coordinates, rather than screen coordinates. Calculating in retinal coordinates is crucial, as it mirrors neuronal adaptation processes that occur locally in the retina, providing a more biologically realistic simulation. Mean eye-tracking precision was estimated at 1.9° during both fixation and pursuit, with 94% of measurements exhibiting an angular error below 5° (see Supplementary Materials).

2.6. Procedure

Participants completed demographic and screening surveys prior to attending the session, which assessed eligibility and collected background information. Upon arrival, they donned the headset and completed HTC’s eye calibration procedure. For a subset of participants ($n = 30$), additional precision checks were conducted using a “follow the dot” task (see Supplementary Materials). Participants unfamiliar with VR were provided extra time to acclimate using a virtual test room and joystick controls.

2.6.1. Training phase To help participants adapt to the spatial distortions introduced by simulated prosthetic vision, a structured training phase was implemented. Training consisted of three sets of five trials with incrementally increasing levels of distortion. Initial trials featured low distortion parameters ($\lambda = 50$, $\rho = 150$) and a pixel-like image rendered using 400 (20×20) electrodes spaced $300 \mu\text{m}$ apart. This provided a large field of view and familiarized participants with the interface. Subsequent trials used a reduced electrode count (100 electrodes in a 10×10 grid) spaced $400 \mu\text{m}$ apart and progressively increased the radial distortion ($\rho = 300$). By the final training level, distortion parameters ($\lambda = 1000$, $\rho = 300$) aligned with realistic values reported for current epiretinal devices (Beyeler et al., 2019), simulating a restricted $\sim 14.6^\circ \times 14.6^\circ$ field of view. Temporal effects, including rasterization, were disabled during training, but gaze-contingent rendering was active to simulate a dynamic viewing experience.

Training began with non-SPV trials (normal vision) before progressing to SPV conditions. Extensive piloting ensured that participants reached 70–90% accuracy in the baseline (non-rastered) condition after training, providing a foundation for consistent performance during the experimental phase.

2.6.2. Experimental phase Participants were randomly assigned to start with either the letter identification task or the motion discrimination task. All participants first completed a baseline condition (“No Raster”), where all electrodes were active on every frame but temporal effects were enabled (see Section 2.5.2). They then proceeded through the four raster conditions (horizontal, vertical, checkerboard, and random) in a counterbalanced order. Each condition comprised 48 trials, divided into six blocks of eight randomized stimuli. Blocks were presented without explicit markers, creating the impression of continuous randomization.

Participants were allowed to abort the session at any time if they felt discomfort or cybersickness. Breaks were offered between blocks, and no participants required intervention. Each session lasted approximately two hours, including training, experimental trials, and debriefing.

2.7. Data collection & analysis

For each trial, we recorded task accuracy, difficulty ratings, and eye/head tracking data.

A linear mixed-effects model was fit to assess the effects of raster pattern, task, and block number on performance, accounting for the repeated-measures design (Magezi, 2015). Following a design-driven maximal approach (Barr et al., 2013), the model included `RasterPattern`, `Task`, and `Block` as fixed effects with full interactions. To capture individual differences, random intercepts and slopes for `Block` and `RasterPattern` were included for each participant: Pairwise post-hoc comparisons were performed to evaluate differences between the checkerboard condition and other raster patterns, with p -values adjusted using the Benjamini–Hochberg procedure to control for multiple comparisons. Model comparisons relied on Akaike and Bayesian information criteria (AIC/BIC) to assess model fit.

$\text{Accuracy} \sim \text{Block} \times \text{RasterStrategy} \times \text{Task} + (1 + \text{Block} + \text{RasterStrategy} \mid \text{Subject}).$

Here, $(1 + \text{Block} + \text{RasterStrategy} \mid \text{Subject})$ indicates random intercepts for each participant plus random slopes for `Block` and `RasterPattern`. Analyses were conducted using the Python `statsmodels` library, with model parameters estimated via restricted maximum likelihood (REML).

Pairwise post-hoc comparisons were performed to evaluate differences between the checkerboard condition and other raster patterns, with p -values adjusted using the Benjamini–Hochberg procedure to control for multiple comparisons. Model comparisons relied on Akaike and Bayesian information criteria (AIC/BIC) to assess model fit.

3. Results

3.1. Checkerboard outperforms other patterns

The checkerboard raster pattern significantly outperformed all other raster strategies across both letter recognition and motion discrimination tasks (Figure 4). By the final block, participants achieved the highest performance with the checkerboard pattern, whereas other raster patterns showed more variable performance, with some participants scoring below chance.

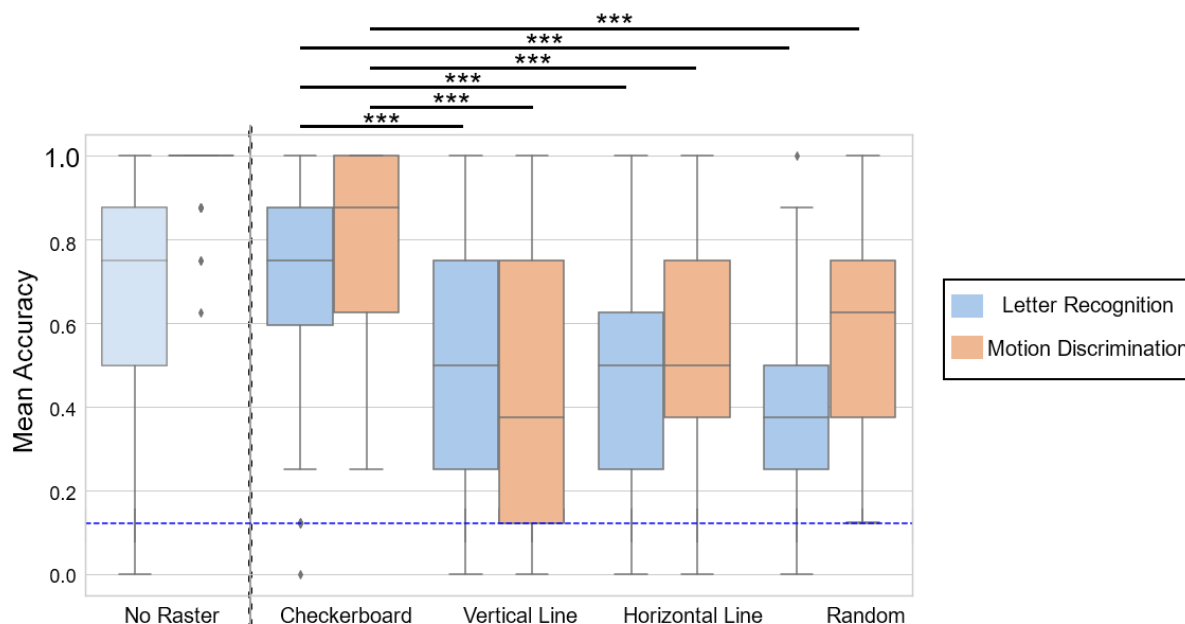


Figure 4: Accuracy by raster pattern. Final block (Block 6) accuracy for both tasks (letter recognition on the left and motion discrimination on the right). The checkerboard pattern significantly outperformed the other raster strategies. The blue dashed line represents chance-level performance (1/8). Significance determined via one-tailed pairwise t-tests with Benjamini–Hochberg correction ($*** = p < .001$).

Participants achieved ceiling-level performance in the “No Raster” motion discrimination condition, with a mean accuracy of 0.969 ± 0.079 , demonstrating the relative simplicity of this task in the absence of raster effects. Across all raster patterns, motion discrimination remained easier than letter recognition, though accuracy was reduced compared to the “No Raster” baseline. For motion discrimination, the checkerboard pattern achieved a mean accuracy of 0.786 ± 0.213 , significantly outperforming vertical (0.450 ± 0.305), horizontal (0.563 ± 0.265), and random (0.591 ± 0.305) raster patterns.

Interestingly, the checkerboard and “No Raster” conditions yielded comparable performance for letter recognition (checkerboard: 0.695 ± 0.260 , baseline: 0.703 ± 0.269), despite participants beginning the study with the “No Raster” condition. The checkerboard pattern’s ability to match “No Raster” performance is particularly

striking given that all other raster strategies incurred a notable performance deficit (vertical: 0.484 ± 0.278 , horizontal: 0.471 ± 0.248), with the random pattern performing worst (0.393 ± 0.246). One-tailed pairwise t -tests were employed to test whether the checkerboard pattern outperformed the other raster patterns. This analysis confirmed the checkerboard pattern’s significant advantage across both tasks ($p < 0.001$ for all comparisons, corrected using the Benjamini–Hochberg procedure).

These findings emphasize the checkerboard pattern’s ability to balance spatial separation and temporal stimulation, enhancing perceptual clarity and task performance compared to less structured raster patterns.

3.2. Performance improvement evident across all conditions

Task performance improved significantly over time for all raster patterns and tasks, reflecting perceptual learning as participants adapted to the challenges of simulated prosthetic vision (Figure 5).

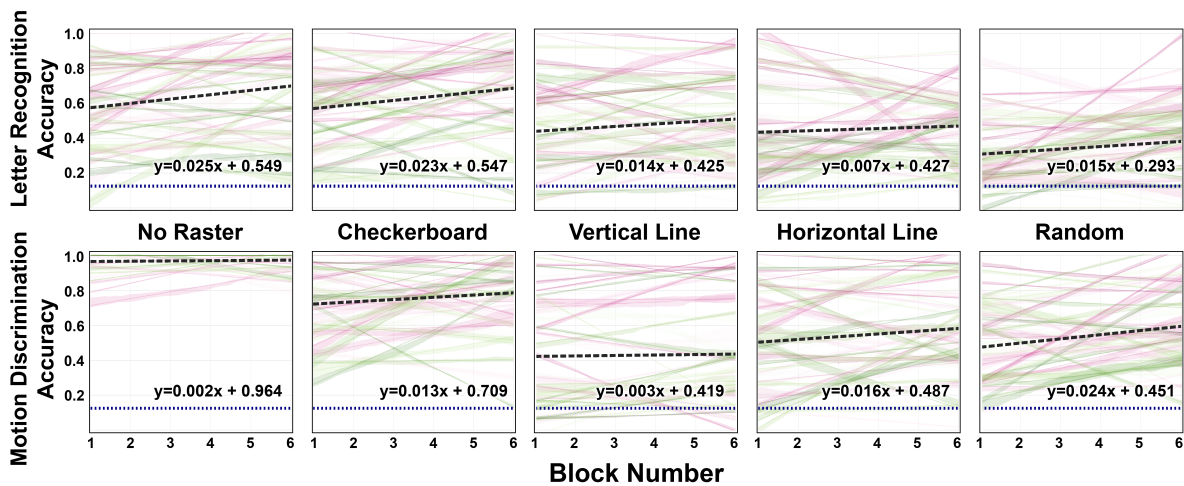


Figure 5: Learning over blocks. Linear mixed-effects model results showing accuracy improvement across six blocks for letter recognition (top) and motion discrimination (bottom). Colored lines represent individual participant fits, and the blue dashed line indicates chance level.

The maximal mixed-effects model identified a significant fixed effect of Block, with accuracy increasing at an average rate of 0.023 per block ($p < .001$, 95% CI = $[0.010, 0.036]$). This improvement was observed across all raster patterns, highlighting the robustness of perceptual learning in adapting to rasterized stimuli.

For the letter recognition task, the checkerboard pattern exhibited the highest fitted offset, indicating superior baseline performance, as well as the steepest fitted slope, suggesting enhanced learning rates compared to other patterns. In the motion discrimination task, the checkerboard pattern again showed the highest offset, but its learning slope was comparable to those of the horizontal and random patterns.

Interestingly, the random pattern exhibited the steepest slope, reflecting rapid adaptation despite its initially lower baseline performance.

Individual participant fits revealed substantial variability, with most participants demonstrating improvement over time. However, some instances of declining performance were observed, potentially reflecting variability in engagement, differences in strategy, or challenges such as fatigue or calibration inconsistencies during longer sessions.

These findings emphasize the checkerboard pattern’s consistent advantages across tasks while underscoring the importance of considering individual differences in future research and prosthetic vision designs.

3.3. Systematic biases depend on stimulus and raster pattern

Participant responses revealed systematic biases influenced by both the stimulus characteristics and the raster pattern (Figure 6).

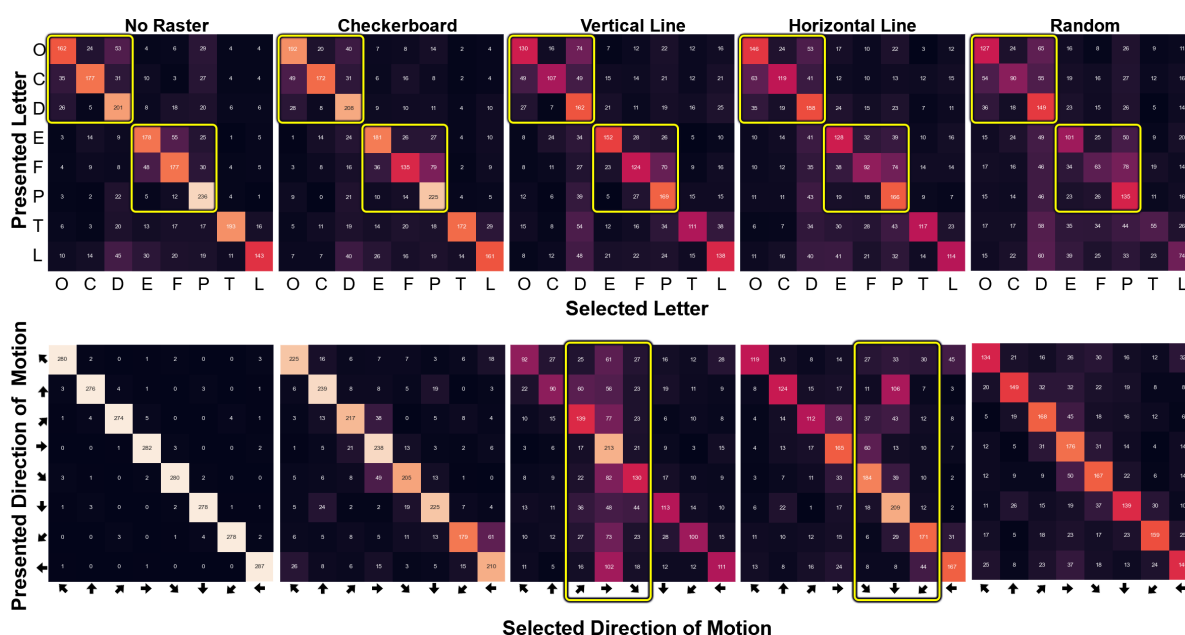


Figure 6: Response bias by stimulus and raster pattern. The letter recognition task (top) exhibited grouping biases for visually similar letters ([C, D, O] and [E, F, P]). In the motion discrimination task (bottom), apparent motion biases emerged for vertical and horizontal raster patterns, favoring the direction of electrode activation. Yellow rectangles highlight expected biases.

In the letter recognition task, participants more frequently confused letters with similar shapes, such as [C, D, O] and [E, F, P], regardless of the raster pattern. The checkerboard and “No Raster” conditions led to the fewest errors, consistent with their higher overall performance. In contrast, the vertical and horizontal patterns resulted in more frequent misidentifications, reflecting the challenges introduced by their respective raster patterns.

In the motion discrimination task, vertical and horizontal patterns introduced biases aligned with the apparent motion of the raster pattern. For the vertical pattern, participants made more errors identifying rightward motion, while the horizontal pattern led to more errors for downward motion. These biases are consistent with the directionality of apparent motion created by the sequential activation of electrode groups in each pattern. Such biases were notably absent in the checkerboard and random conditions, highlighting their robustness in preserving unbiased perceptual interpretation.

Across both tasks, the letters D and P were most frequently selected when participants made incorrect guesses. This may reflect an artifact of the joystick mapping, as D and P were associated with forward and backward joystick motions. These movements may have been perceived as more intuitive or easier to execute, leading participants to default to these choices when uncertain.

In sum, these results illustrate how both stimulus characteristics and raster patterns shape perceptual biases, further supporting the checkerboard pattern’s advantages in minimizing errors and providing a more stable perceptual experience.

3.4. Self-reported difficulty ratings mirror performance trends

Participants’ difficulty ratings mirrored their performance, with conditions yielding higher accuracy generally rated as easier (Figure 7).

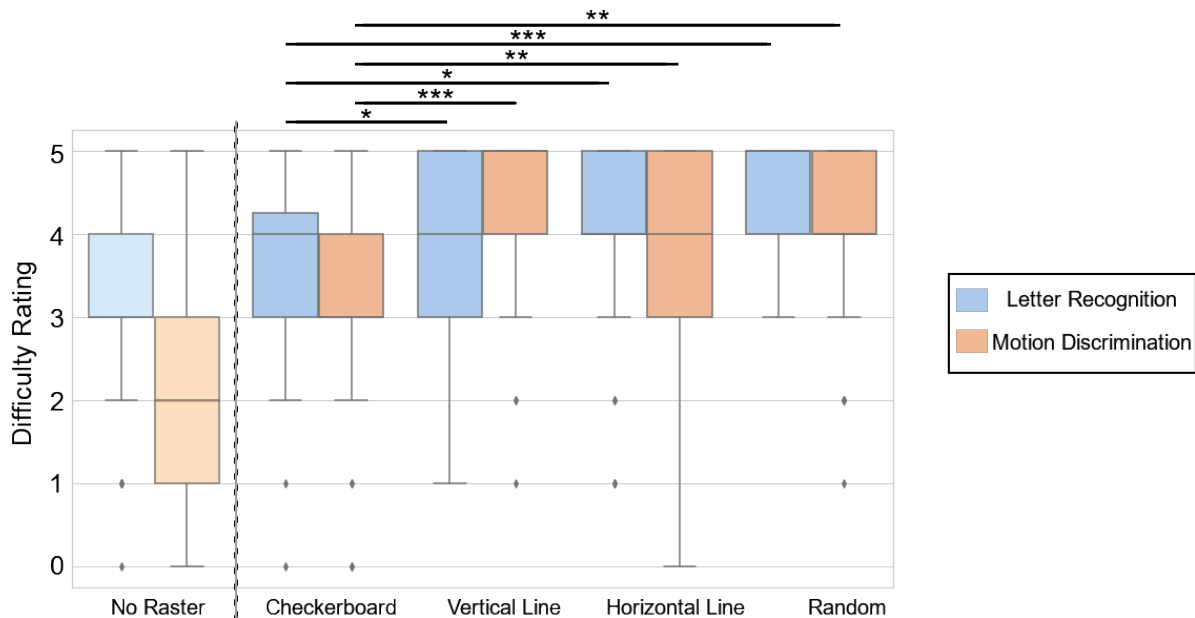


Figure 7: Difficulty Ratings. Mean difficulty ratings (1 = low difficulty, 5 = high difficulty) for letter recognition (left) and motion discrimination (right). Ratings align with performance, with the checkerboard condition rated as significantly easier than vertical, horizontal, and random patterns. Significance determined via one-tailed pairwise t-tests with Benjamini–Hochberg correction ($= p < .05$, $= p < .01$, $= p < .001$).

In the letter recognition task, the checkerboard and “No Raster” conditions were rated as the least difficult, while the vertical, horizontal, and random patterns were rated significantly more challenging. For the motion discrimination task, the “No Raster” condition received the lowest difficulty ratings, followed by the checkerboard condition, which was still rated as substantially easier than the other raster patterns.

These results highlight the checkerboard pattern’s ability to enhance both objective performance and subjective usability, emphasizing its potential as a candidate for future prosthetic vision designs.

4. Discussion

This study systematically evaluated four raster patterns in a simulated prosthetic vision environment, focusing on letter recognition and motion discrimination tasks.

The checkerboard raster pattern consistently outperformed the other patterns, yielding higher accuracy and lower difficulty ratings across both tasks. By maximizing the spatial separation of activated electrodes, the checkerboard pattern effectively reduced interference between phosphenes, enhancing perceptual clarity and task performance. These results highlight the checkerboard pattern’s ability to balance spatial and temporal stimulation, achieving performance levels comparable to the unstructured “No Raster” condition while adhering to regulatory safety constraints.

This work fills a critical gap in the literature by providing the first systematic assessment of raster patterns and offering evidence-based insights for the design of high-resolution visual neuroprostheses.

4.1. Checkerboard raster enhances performance and usability

The spatial arrangement of electrode activation was critical for optimizing performance in both letter recognition and motion discrimination tasks. The checkerboard pattern demonstrated superior accuracy (Figure 4), supporting the hypothesis that maximizing spatial separation between activated electrodes reduces perceptual interference. This finding aligns with prior studies showing that closely spaced phosphenes often merge, complicating the recognition of complex shapes like letters (Horsager et al., 2010; Wilke et al., 2011; Bosking et al., 2022; Hou et al., 2024a).

Interestingly, the checkerboard pattern also excelled in the motion discrimination task, where other patterns, such as vertical and horizontal rasters, introduced apparent motion biases due to their sequential activation order. These biases were absent in the checkerboard pattern, indicating that its spatial organization mitigates the perceptual artifacts that can result from raster-induced motion.

Participants’ self-reported difficulty ratings further underscored the checkerboard pattern’s advantages (Figure 7). Lower difficulty ratings in both tasks suggest that this pattern not only enhances performance but also improves the subjective user experience,

which is essential for promoting device usability and adoption (Beyeler and Sanchez-Garcia, 2022; Kasowski et al., 2023; Nadolskis et al., 2024).

4.2. Limitations

While this study highlights the advantages of the checkerboard raster pattern, several limitations must be acknowledged.

First, although devices like the Argus II operate at millisecond-level temporal resolution, achieving such rapid rastering was not feasible with the current head-mounted display setup. We adopted a raster frequency of approximately 5 Hz, balancing feasibility with realism for larger, high-electrode-count devices envisioned for the near future. This choice ensures generalizability but may not fully replicate the temporal dynamics of existing systems.

Second, the study relied on simulated prosthetic vision with sighted participants and idealized phosphene models (Beyeler et al., 2019; Granley and Beyeler, 2021; Horsager et al., 2009). While this approach facilitates controlled experimentation, it does not account for the complex electrode interactions or neural adaptation observed in real prosthesis users (Wilke et al., 2011; Pérez Fornos et al., 2012). Validating these findings with prosthesis users remains an essential next step.

Finally, the chosen tasks—letter recognition and motion discrimination—capture specific aspects of functional vision but do not encompass the full range of challenges faced by prosthesis users. Including tasks like navigation, object recognition, and dynamic scene analysis (Geruschat et al., 2015) could provide a more comprehensive evaluation of raster patterns.

4.3. Future directions

The findings from this study provide a foundation for optimizing raster patterns in visual prostheses and suggest promising directions for future research.

The checkerboard raster pattern consistently demonstrated superior performance across tasks, reducing perceptual interference and avoiding the apparent motion biases seen with vertical and horizontal patterns. This result underscores its potential as a design principle for next-generation prosthetic devices, particularly those with high electrode counts. Future work should investigate how the checkerboard pattern performs under more realistic temporal resolutions and with advanced device features, such as gaze-contingent updates and dynamic stimulation strategies.

Beyond validating these results with prosthesis users, expanding to more complex and ecologically valid tasks will help bridge the gap between controlled simulations and real-world usability. Investigating the interplay between raster patterns, electrode density, and field of view could reveal additional insights into optimizing stimulation strategies for practical use.

Finally, this study highlighted substantial individual variability in performance and learning rates. Developing adaptive training paradigms tailored to users' cognitive and

behavioral strategies could further enhance device usability, ensuring that advancements in electrode activation strategies translate into meaningful functional outcomes for individuals living with profound blindness.

Acknowledgments

This work was supported by the National Eye Institute of the National Institutes of Health under Award Number R00-EY029329. The content is solely the responsibility of the authors and does not necessarily represent the official views of the National Institutes of Health.

Data Availability

The raw data for this study is publicly available on the Open Science Framework at <https://osf.io/nm6aw/>. Prosthetic vision simulations were generated with BionicVisionXR (Kasowski and Beyeler, 2022), an open-source Unity toolbox available at <https://github.com/bionicvisionlab/BionicVisionXR>.

References

- Avraham, D., Jung, J., Yitzhaky, Y., and Peli, E. (2021). Retinal prosthetic vision simulation: temporal aspects. *Journal of Neural Engineering*.
- Barr, D. J., Levy, R., Scheepers, C., and Tily, H. J. (2013). Random effects structure for confirmatory hypothesis testing: Keep it maximal. *Journal of Memory and Language*, 68(3):255–278.
- Beyeler, M., Boynton, G., Fine, I., and Rokem, A. (2017a). pulse2percept: A Python-based simulation framework for bionic vision. In *Proceedings of the 16th Python in Science Conference*, pages 81–88, Austin, Texas. SciPy.
- Beyeler, M., Nanduri, D., Weiland, J. D., Rokem, A., Boynton, G. M., and Fine, I. (2019). A model of ganglion axon pathways accounts for percepts elicited by retinal implants. *Scientific Reports*, 9(1):1–16.
- Beyeler, M., Rokem, A., Boynton, G. M., and Fine, I. (2017b). Learning to see again: biological constraints on cortical plasticity and the implications for sight restoration technologies. *Journal of Neural Engineering*, 14(5):051003.
- Beyeler, M. and Sanchez-Garcia, M. (2022). Towards a Smart Bionic Eye: AI-powered artificial vision for the treatment of incurable blindness. *Journal of Neural Engineering*, 19(6):063001. Publisher: IOP Publishing.
- Bosking, W. H., Oswalt, D. N., Foster, B. L., Sun, P., Beauchamp, M. S., and Yoshor, D. (2022). Percepts evoked by multi-electrode stimulation of human visual cortex. *Brain Stimulation*, 15(5):1163–1177.
- Chen, X., Wang, F., Fernandez, E., and Roelfsema, P. R. (2020). Shape perception via a high-channel-count neuroprosthesis in monkey visual cortex. *Science*, 370(6521):1191–1196. Publisher: American Association for the Advancement of Science Section: Research Article.
- Cruz, L. d., Coley, B. F., Dorn, J., Merlini, F., Filley, E., Christopher, P., Chen, F. K., Wuyyuru, V., Sahel, J., Stanga, P., Humayun, M., Greenberg, R. J., Dagnelie, G., and Group, f. t. A. I. S. (2013). The Argus II epiretinal prosthesis system allows letter and word reading and long-term function in patients with profound vision loss. *British Journal of Ophthalmology*, 97(5):632–636. Publisher: BMJ Publishing Group Ltd Section: Clinical science.
- da Cruz, L., Fynes, K., Georgiadis, O., Kerby, J., Luo, Y. H., Ahmado, A., Vernon, A., Daniels, J. T., Nommiste, B., Hasan, S. M., Gooljar, S. B., Carr, A.-J. F., Vugler, A., Ramsden, C. M., Bictash, M., Fenster, M., Steer, J., Harbinson, T., Wilbrey, A., Tufail, A., Feng, G., Whitlock, M., Robson, A. G., Holder, G. E., Sagoo, M. S., Loudon, P. T., Whiting, P., and Coffey, P. J. (2018). Phase 1 clinical study of an embryonic stem cell-derived retinal pigment epithelium patch in age-related macular degeneration. *Nature Biotechnology*, 36(4):328–337.
- Dagnelie, G., Keane, P., Narla, V., Yang, L., Weiland, J., and Humayun, M. (2007).

- Real and virtual mobility performance in simulated prosthetic vision. *Journal of Neural Engineering*, 4(1):S92.
- Dorn, J. D., Ahuja, A. K., Caspi, A., da Cruz, L., Dagnelie, G., Sahel, J. A., Greenberg, R. J., McMahon, M. J., and Grp, A. I. S. (2013). The Detection of Motion by Blind Subjects With the Epiretinal 60-Electrode (Argus II) Retinal Prosthesis. *Jama Ophthalmology*, 131(2):183–189.
- Efron, R. (1973). Conservation of temporal information by perceptual systems. *Perception & Psychophysics*, 14(3):518–530.
- Fernandez, E. (2018). Development of visual Neuroprostheses: trends and challenges. *Bioelectronic Medicine*, 4(1):12.
- Geruschat, D. R., Flax, M., Tanna, N., Bianchi, M., Fisher, A., Goldschmidt, M., Fisher, L., Dagnelie, G., Deremeik, J., Smith, A., Anafloos, F., and Dorn, J. (2015). FLORA™: Phase I development of a functional vision assessment for prosthetic vision users. *Clinical and Experimental Optometry*, 98(4):342–347.
- Granley, J. and Beyeler, M. (2021). A Computational Model of Phosphene Appearance for Epiretinal Prostheses. In *2021 43rd Annual International Conference of the IEEE Engineering in Medicine Biology Society (EMBC)*, pages 4477–4481. ISSN: 2694-0604.
- Hamel, C. (2006). Retinitis pigmentosa. *Orphanet Journal of Rare Diseases*, 1(1):40.
- Han, N., Srivastava, S., Xu, A., Klein, D., and Beyeler, M. (2021). Deep Learning–Based Scene Simplification for Bionic Vision. In *Augmented Humans Conference 2021, AHs’21*, pages 45–54, New York, NY, USA. Association for Computing Machinery.
- Hayes, J. S., Yin, V. T., Piyathaisere, D., Weiland, J. D., Humayun, M. S., and Dagnelie, G. (2003). Visually guided performance of simple tasks using simulated prosthetic vision. *Artif Organs*, 27(11):1016–28.
- Horsager, A., Greenberg, R. J., and Fine, I. (2010). Spatiotemporal Interactions in Retinal Prosthesis Subjects. *Investigative Ophthalmology & Visual Science*, 51(2):1223–1233.
- Horsager, A., Greenwald, S. H., Weiland, J. D., Humayun, M. S., Greenberg, R. J., McMahon, M. J., Boynton, G. M., and Fine, I. (2009). Predicting Visual Sensitivity in Retinal Prosthesis Patients. *Investigative Ophthalmology & Visual Science*, 50(4):1483–1491.
- Hou, Y., Nanduri, D., Granley, J., Weiland, J. D., and Beyeler, M. (2024a). Axonal stimulation affects the linear summation of single-point perception in three Argus II users. *Journal of Neural Engineering*, 21(2):026031. Publisher: IOP Publishing.
- Hou, Y., Pullela, L., Su, J., Aluru, S., Sista, S., Lu, X., and Beyeler, M. (2024b). Predicting the Temporal Dynamics of Prosthetic Vision. In *2024 46th Annual International Conference of the IEEE Engineering in Medicine and Biology Society (EMBC)*, pages 1–4. ISSN: 2694-0604.
- Jung, T., Zeng, N., Fabbri, J. D., Eichler, G., Li, Z., Willeke, K., Wingel, K. E., Dubey, A., Huq, R., Sharma, M., Hu, Y., Ramakrishnan, G., Tien, K., Mantovani,

- P., Parihar, A., Yin, H., Oswalt, D., Misdorp, A., Uguz, I., Shinn, T., Rodriguez, G. J., Nealley, C., Gonzales, I., Roukes, M., Knecht, J., Yoshor, D., Canoll, P., Spinazzi, E., Carloni, L. P., Pesaran, B., Patel, S., Youngerman, B., Cotton, R. J., Tolia, A., and Shepard, K. L. (2024). Stable, chronic in-vivo recordings from a fully wireless subdural-contained 65,536-electrode brain-computer interface device. Pages: 2024.05.17.594333 Section: New Results.
- Kasowski, J. and Beyeler, M. (2022). Immersive Virtual Reality Simulations of Bionic Vision. In *Augmented Humans 2022*, pages 82–93, Kashiwa, Chiba Japan. ACM.
- Kasowski, J., Johnson, B. A., Neydavood, R., Akkaraju, A., and Beyeler, M. (2023). A systematic review of extended reality (XR) for understanding and augmenting vision loss. *Journal of Vision*, 23(5):5.
- Lorach, H., Goetz, G., Smith, R., Lei, X., Mandel, Y., Kamins, T., Mathieson, K., Huie, P., Harris, J., Sher, A., and Palanker, D. (2015). Photovoltaic restoration of sight with high visual acuity. *Nat Med*, 21(5):476–82.
- Luo, Y. H. and da Cruz, L. (2016). The Argus((R)) II Retinal Prosthesis System. *Prog Retin Eye Res*, 50:89–107.
- Magezi, D. A. (2015). Linear mixed-effects models for within-participant psychology experiments: an introductory tutorial and free, graphical user interface (LMMgui). *Frontiers in Psychology*, 6.
- Musk, E. and Neuralink (2019). An Integrated Brain-Machine Interface Platform With Thousands of Channels. *Journal of Medical Internet Research*, 21(10):e16194. Company: Journal of Medical Internet Research Distributor: Journal of Medical Internet Research Institution: Journal of Medical Internet Research Label: Journal of Medical Internet Research Publisher: JMIR Publications Inc., Toronto, Canada.
- Nadolskis, L., Turkstra, L. M., Larnyo, E., and Beyeler, M. (2024). Aligning Visual Prosthetic Development With Implantee Needs. *Translational Vision Science & Technology*, 13(11):28.
- Palanker, D., Le Mer, Y., Mohand-Said, S., Muqit, M., and Sahel, J. A. (2020). Photovoltaic Restoration of Central Vision in Atrophic Age-Related Macular Degeneration. *Ophthalmology*.
- Parikh, N., Itti, L., and Weiland, J. (2010). Saliency-based image processing for retinal prostheses. *Journal of Neural Engineering*, 7(1):016006. Publisher: IOP Publishing.
- Prem Senthil, M., Khadka, J., and Pesudovs, K. (2017). Seeing through their eyes: lived experiences of people with retinitis pigmentosa. *Eye*, 31(5):741–748. Publisher: Nature Publishing Group.
- Pérez Fornos, A., Sommerhalder, J., da Cruz, L., Sahel, J. A., Mohand-Said, S., Hafezi, F., and Pelizzone, M. (2012). Temporal Properties of Visual Perception on Electrical Stimulation of the Retina. *Investigative Ophthalmology & Visual Science*, 53(6):2720–2731.

- Rashbass, C. (1970). The visibility of transient changes of luminance. *The Journal of Physiology*, 210(1):165–186.
- Rizzo, III, J. F., Wyatt, J., Loewenstein, J., Kelly, S., and Shire, D. (2003). Perceptual Efficacy of Electrical Stimulation of Human Retina with a Microelectrode Array during Short-Term Surgical Trials. *Investigative Ophthalmology & Visual Science*, 44(12):5362–5369.
- Russell, S., Bennett, J., Wellman, J. A., Chung, D. C., Yu, Z.-F., Tillman, A., Wittes, J., Pappas, J., Elci, O., McCague, S., Cross, D., Marshall, K. A., Walshire, J., Kehoe, T. L., Reichert, H., Davis, M., Raffini, L., George, L. A., Hudson, F. P., Dingfield, L., Zhu, X., Haller, J. A., Sohn, E. H., Mahajan, V. B., Pfeifer, W., Weckmann, M., Johnson, C., Gewaily, D., Drack, A., Stone, E., Wachtel, K., Simonelli, F., Leroy, B. P., Wright, J. F., High, K. A., and Maguire, A. M. (2017). Efficacy and safety of voretigene neparvovec (AAV2-hRPE65v2) in patients with RPE65-mediated inherited retinal dystrophy: a randomised, controlled, open-label, phase 3 trial. *The Lancet*, 390(10097):849–860. Publisher: Elsevier.
- Sainohira, M., Yamashita, T., Terasaki, H., Sonoda, S., Miyata, K., Murakami, Y., Ikeda, Y., Morimoto, T., Endo, T., Fujikado, T., Kamo, J., and Sakamoto, T. (2018). Quantitative analyses of factors related to anxiety and depression in patients with retinitis pigmentosa. *PloS One*, 13(4):e0195983.
- Sanchez-Garcia, M., Martinez-Cantin, R., and Guerrero, J. J. (2020). Semantic and structural image segmentation for prosthetic vision. *PLOS ONE*, 15(1):e0227677.
- Second Sight (2013). *Argus® II Retinal Prosthesis System Surgeon Manual*. Number 900029-001 Rev C. Second Sight Medical Products, Inc., Sylmar, CA.
- Vergniewx, V., Macé, M. J.-M., and Jouffrais, C. (2017). Simplification of Visual Rendering in Simulated Prosthetic Vision Facilitates Navigation. *Artificial Organs*, 41(9):852–861. Publisher: John Wiley & Sons, Ltd.
- Weiland, J. D., Walston, S. T., and Humayun, M. S. (2016). Electrical Stimulation of the Retina to Produce Artificial Vision. *Annual Review of Vision Science*, 2(1):273–294.
- Wilke, R. G. H., Moghadam, G. K., Lovell, N. H., Suaning, G. J., and Dokos, S. (2011). Electric crosstalk impairs spatial resolution of multi-electrode arrays in retinal implants*. *Journal of Neural Engineering*, 8(4):046016.
- Yücel, E. I., Sadeghi, R., Kartha, A., Montezuma, S. R., Dagnelie, G., Rokem, A., Boynton, G. M., Fine, I., and Beyeler, M. (2022). Factors affecting two-point discrimination in Argus II patients. *Frontiers in Neuroscience*, 16:901337.

Appendix A. Eye-Tracking Accuracy of the HTC Vive Pro

To assess the precision of the HTC Vive Pro’s built-in eye tracker, $n = 30$ participants tracked a moving on-screen dot ($\sim 2.4^\circ$ visual angle) using their eyes. The dot moved randomly between four corners positioned halfway between the center and edges of the screen. It traversed the distance between points over 2.5 ± 0.5 seconds and remained stationary at each location for 1.5 seconds.

The angular error, defined as the distance between the dot’s center and the user’s gaze location, was measured every 0.1 s. Measurements were taken during both fixation (when the dot was stationary) and pursuit (when it was moving). Mean angular error was $1.904(2048)^\circ$ during fixation and $1.838(1660)^\circ$ during pursuit, with no significant difference between the two conditions (t-test for non-equal variances, $p > 0.27$).

Overall, 94.1% of measurements had an angular error below 5° , and 80% were below 3° . These results indicate that the HTC Vive Pro provides adequate precision for gaze-contingent rendering in simulated prosthetic vision experiments (Figure A1).

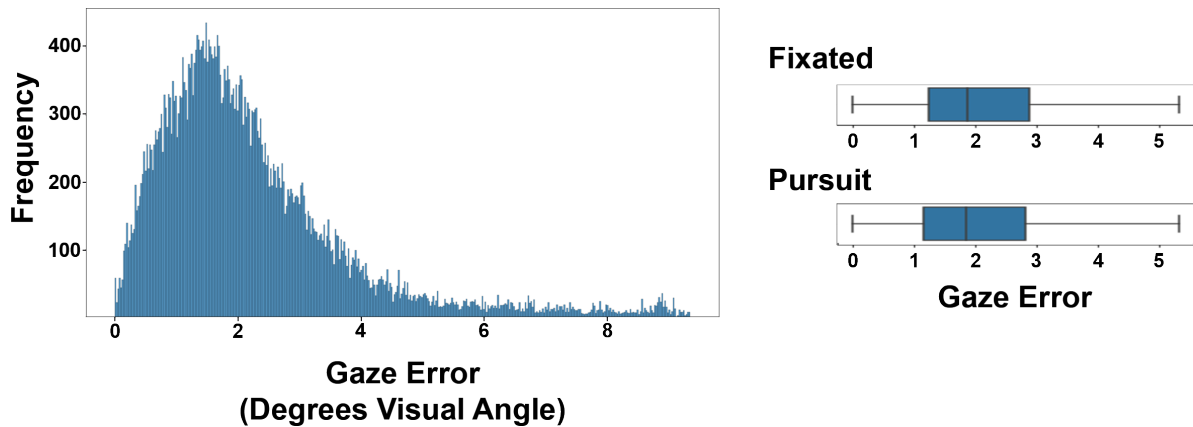


Figure A1: Eye tracking accuracy of the HTC Vive Pro. The histogram (left) shows the distribution of angular gaze error (degrees visual angle) across all measurements, with most errors falling below 5° . The boxplots (right) compare gaze error during fixation (when the dot was stationary) and pursuit (when the dot was moving). Mean errors were similar across conditions ($1.904(2048)^\circ$ for fixation and $1.838(1660)^\circ$ for pursuit), with no significant difference between the two (t-test, $p > 0.27$). Over 94% of measurements had an error below 5° , confirming the system’s precision for gaze-contingent rendering.